physica status solidi rrl
www.pss-rapid.com

Ferroelectric $SrMnO_3$ Thin Film Grown on (110)-Oriented PMN-PT Substrate

Seong Min Park, Jaegyu Kim, Gopinathan Anoop, WooJun Seol, Su Yong Lee, Hyunjin Joh, Tae Yeon Kim, Je Oh Choi, Seungbum Hong, Chan-Ho Yang, Hyeon Jun Lee, and Ji Young Jo**

Exploring the unique physical properties of oxide perovskites necessitates their growth on diverse single-crystal substrates. The thin-film growth of perovskite $SrMnO_3$ (SMO) has been a particular focus of research due to its emerging room-temperature multiferroicity. Herein, the epitaxial thin films of (110)-oriented SMO are grown on the piezoelectric (110)-oriented $(1-x)Pb(Mg_{1/3}Nb_{2/3})O_3-xPbTiO_3$ (PMN-PT) substrate. The effects of the thickness and oxygen annealing on the crystal structure, stoichiometry, and ferroelectric properties of the SMO thin film are systematically investigated. The tensile strain produced by the lattice mismatch between the bulk SMO and the PMN-PT substrate causes an expansion of the *c*-lattice parallel to the in-plane direction of the substrate. The films show larger *a*-, *b*-, and *c*-lattice parameters than the bulk material, resulting in volume expansion of the unit cell. This lattice expansion is attributed to the generation of oxygen vacancies driven by the reduced formation energy caused by the high elastic strain. Piezoelectric force microscopy reveals that the SMO film contains domains with strain-mediated in-plane and vacancy-mediated out-of-plane polarization. Furthermore, the piezoelectric response of the PMN-PT substrate effectively modulates the biaxial tensile strain in the SMO film, offering a potential strategy for controlling the crystal structure and ferroelectric properties of SMO.

1. Introduction

Perovskite oxides have been widely studied because of their emerging multiferroicity exhibiting ferroelectricity and magnetic order simultaneously.[1–5] As a crucial criterion, a higher magnetic transition temperature has been investigated in engineered perovskite alkaline earth manganite systems.[6,7] Antiferromagnetic-paraelectric $SrMnO_3$ (SMO) is a particularly promising system for multiferroic ordering at room temperature.[8,9] An expansion in the lattice of the perovskite SMO can drive the off-centering of the magnetic Mn^{4+} ion, and thus, the ferroelectric phase at room temperature.[10] In bulk SMO, the partial replacement of Sr with Ba ions results in lattice expansion and induces a strain-mediated ferroelectric phase.[11] The growth of single-crystal films on substrates with different lattice parameters, termed strain engineering, is an alternative strategy for inducing or improving ferroelectricity.[12] The density functional theory (DFT) has predicted the polar phase of SMO with polarization along the [001] and [110] direction under $<-1.4\%$ epitaxial compressive strain and $>1\%$ tensile strain,

S. M. Park, G. Anoop, W. J. Seol, H. Joh, T. Y. Kim, J. O. Choi, J. Y. Jo
School of Materials Science and Engineering
Gwangju Institute of Science and Technology
Gwangju 61005, South Korea
E-mail: jyjo@gist.ac.kr

J. Kim, S. Hong
Department of Materials Science and Engineering
Korea Advanced Institute of Science and Technology
Daejeon 34141, South Korea

The ORCID identification number(s) for the author(s) of this article can be found under https://doi.org/10.1002/pssr.202400025.

DOI: 10.1002/pssr.202400025

J. Kim, C.-H. Yang
Department of Physics
Korea Advanced Institute of Science and Technology
Daejeon 34141, South Korea

G. Anoop
Department of Physics
Amrita Vishwa Vidyapeetham
Amritapuri 690525, India

S. Y. Lee
Pohang Accelerator Laboratory
Pohang University of Science and Technology
Pohang 37673, South Korea

H. J. Lee
Department of Materials Science and Engineering
Kangwon National University
Samcheok 25913, South Korea
E-mail: hjlee.mse@kangwon.ac.kr

respectively.[8] Therefore, an adequate choice of substrate can stabilize the polar state and control the direction of polarization.

For a decade, most experimental studies on epitaxial SMO film growth have been limited to using only few conventional perovskite substrates with typical crystal orientation, such as (001)-oriented $LaSrAlO_4$ (LSAO), $LaAlO_3$ (LAO), $(La_{0.3}Sr_{0.7})(Al_{0.65}Ta_{0.35})O_3$ (LSAT), $SrTiO_3$ (STO), and (110)-oriented $DsScO_3$ (DSO) substrate.[13–16] Among these, the SMO films grown on LSAT and DSO substrates under 1.79% and 3.68% tensile strain, respectively, exhibited ferroelectric properties, whereas the film grown on the STO substrate under 2.76% tensile strain did not.[15,16] This anomaly indicates that variables other than the epitaxial strain, which occur during thin-film growth, can also induce ferroelectricity. For example, oxygen vacancies produced due to biaxial tensile strain can result in the modification of the polar orders.[10] Research on the deposition and characterization of thin films on previously unexplored substrates can open a path for discovering novel phases and understanding the effects of misfit strain and other variables, including crystal structure and defect chemistry, on their properties.[17–19]

As a candidate for functional substrate, piezoelectric materials are currently attracting attention because the piezoelectric distortion of the substrate can induce changes in the biaxial strain of thin films in real time.[20–22] $(1–x)Pb(Mg_{1/3}Nb_{2/3})O_3–xPbTiO_3$ (PMN-PT), a well-known relaxor ferroelectric perovskite material, has been widely used as a piezoelectric substrate owing to its high piezoelectricity.[23] However, the growth of single-crystal SMO films on PMN-PT substrate is challenging because of the significant lattice mismatch between the bulk SMO and PMN-PT substrate (>5.79%).[24–28] The growth of single-crystal SMO films on piezoelectric PMN-PT substrates requires a buffer layer to relax the elastic energy inside the SMO film and optimize the growth conditions to maintain the perovskite crystal structure. A systematic investigation of the interplay between strain, defects, crystal structure, and polar states is essential to provide insight into the structure–property relationship.

In this study, we grew a single-crystal (110)-oriented SMO thin film on a $(La_{0.7}Sr_{0.3})MnO_3$ (LSMO)-buffered PMN-PT substrate using pulsed laser deposition (PLD) to investigate the effect of strain and oxygen vacancies on the structural and ferroelectric properties. We chose the (110)-oriented PMN-PT, which has the largest converse piezoelectric effect owing to its high electromechanical coupling with polarization rotation in the rhombohedral structure.[29] The effects of the growth conditions, including oxygen partial pressure and film thickness, on the crystal structure of the SMO film were systematically studied using X-ray diffraction (XRD). X-ray photoelectron spectroscopy (XPS) and electron energy loss spectroscopy (EELS) were used to investigate the oxygen stoichiometry of the SMO film. Unlike previously predicted and demonstrated tensile-strained SMO films with in-plane polarization,[13,15] the SMO film grown on the LSMO-buffered PMN-PT substrate exhibited a piezoelectric response in both the lateral and vertical directions. The hysteresis loops of the piezoelectric force microscopy (PFM) out-of-plane amplitude and phase indicate that the SMO film has ferroelectricity with the polarization rotating toward the surface-normal direction. In situ XRD revealed that the electric field-induced piezoelectric strain of the PMN-PT substrate was transferred to the SMO film, resulting in a change in the biaxial strain.

2. Results and Discussion

Single-crystal $SrMnO_3$ (SMO) thin films with a $(110)_{pc}$-orientation were grown on the $(La_{0.7}Sr_{0.3})MnO_3$ (LSMO) buffer layer and $(1–x)Pb(Mg_{1/3}Nb_{2/3})O_3–xPbTiO_3$ (PMN-PT) substrate. The SMO films were annealed under the oxygen atmosphere of 760 Torr at 350 °C to minimize leakage current and oxygen vacancies ($V_O^{\cdot\cdot}$).[30] Before annealing the as-grown SMO films, the $SrRuO_3$ (SRO) capping layer was deposited on the surface of the film for selective oxygen annealing.[15] Through the post-annealing with SRO capping layer, the leakage current density (Figure S1, Supporting Information) and $V_O^{\cdot\cdot}$ concentration (Figure S2, Supporting Information) of the as-grown SMO films were effectively reduced. The difference in XRD patterns measured before and after postannealing was negligible, indicating that conventional XRD was limited to investigating the effect of postannealing on the crystal structure (Figure S3, Supporting Information). The SRO capping layer was removed after annealing to avoid unexpected extrinsic effects such as structural deformation. The XRD patterns measured after the capping layer removal were similar to the patterns measured with the capping layer (Figure S4, Supporting Information). The coupled theta-2theta scan exhibits distinct (110) diffraction patterns of LSMO and SMO films without the generation of a secondary phase, indicating that both films are $(110)_{pc}$-oriented single-crystals, as shown in **Figure 1**a. A schematic of the SMO/LSMO/PMN-PT heterostructure is shown in the inset of Figure 1a. An LSMO film was used as the bottom electrode of the SMO capacitor. This LSMO bottom electrode also plays a role in reducing the misfit strain between PMN-PT substrate and SMO film from 5.79% to 2%.

To understand the effect of the oxygen partial pressure (P_{O_2}) on crystallinity, XRD patterns of the SMO films grown under various P_{O_2} values (1, 10, 50, and 100 mTorr) were measured, as shown in Figure 1b. The normalized integrated intensity of the $(110)_{pc}$ reflection of the SMO film grown at 1 mTorr was six times larger than that of the film grown at 100 mTorr, although they had similar film thicknesses of approximately 100 nm. We found a slightly decreased integrated intensity for the SMO film grown at P_{O_2} lower than 1 mTorr, indicating that growth at 1 mTorr provided the highest crystallinity in this study.

We investigated the thickness-dependent crystal structure of the SMO film by measuring the XRD profiles of the SMO films with thicknesses of 85, 113, and 142 nm grown at $P_{O_2} = 1$ mTorr, as shown in Figure 1c. The peak positions of $(110)_{pc}$ reflection of 85, 113, and 142 nm thick films are 26.41°, 26.40°, and 26.39°, corresponding to out-of-plane interplanar spacing termed as $d_{(110)}$-spacing of 2.713, 2.714, and 2.715 Å, respectively. The increase in $d_{(110)}$-spacing with increasing film thickness under biaxial tensile strain can be as attributed to strain relaxation. To get more information on crystallinity, we extracted the intensity profile along the in-plane $[-110]_{pc}$ scattering vector from the coupled theta-2theta scan using two-dimensional detector (Figure S5, Supporting Information). The SMO film with a thickness of 142 nm exhibits a narrower full width at half maximum

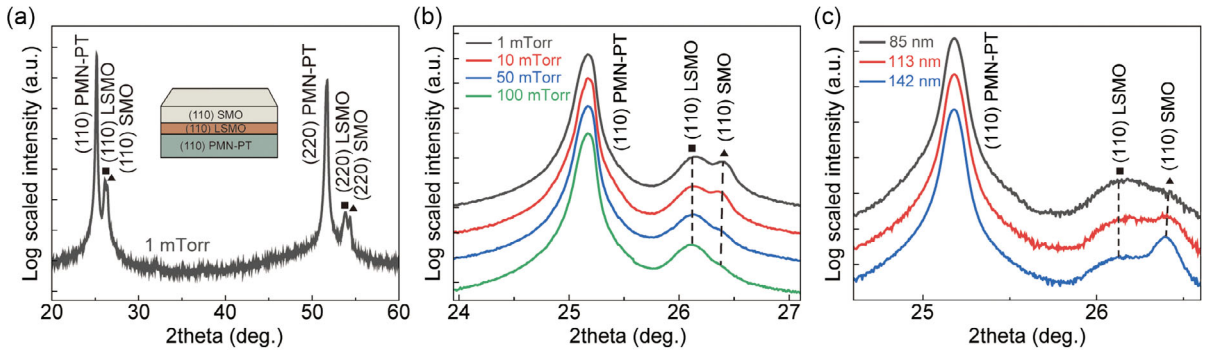

Figure 1. a) Coupled theta-2theta XRD scan for the SMO/LSMO/PMN-PT heterostructure grown at $P_{O_2} = 1$ mTorr. The inset is the schematic illustration of the heterostructure. The out-of-plane diffraction profiles near $(110)_{pc}$ reflection (*pc* denotes pseudocubic indices) for SMO/LSMO/PMN-PT heterostructure b) with the various P_{O_2} (1, 10, 50, and 100 mTorr) and c) with the different thickness (*t*SMO = 85, 113, and 142 nm) grown at $P_{O_2} = 1$ mTorr.

(FWHM) value (0.900°) compared to the 85 nm thick SMO film (1.087°). This suggests that the thicker SMO film is more $(110)_{pc}$-textured and has higher crystallinity than its thinner counterpart. As partial strain relaxation occurs over the critical thickness, typically reported as below 35 nm,[27] the decrease of FWHM value is attributed to the strain relaxation with an increase in the film thickness.

Asymmetric reciprocal space maps (RSMs) provided further information on the lattice parameters of the SMO films. We measured the RSMs near the $(321)_{pc}$ reflection of the SMO film, as shown in **Figure 2**a–c, allowing us to measure both *a*- and *c*-lattice parameters simultaneously. We set the in-plane scattering vectors Q_x and Q_y parallel to the $[001]_{pc}$-axis and the $[-110]_{pc}$-axis of the (110)-oriented SMO film, respectively, whereas the out-of-plane scattering vector Q_z was set parallel to the $[110]_{pc}$-axis. Detailed information on the estimation of the lattice parameters from XRD is provided in the Supporting Information (Figure S6, Supporting Information). Figure 2d shows the relationship of lattice axes (*a*, *b*, and *c*) of the $(110)_{pc}$-oriented unit cell between substrate and films.

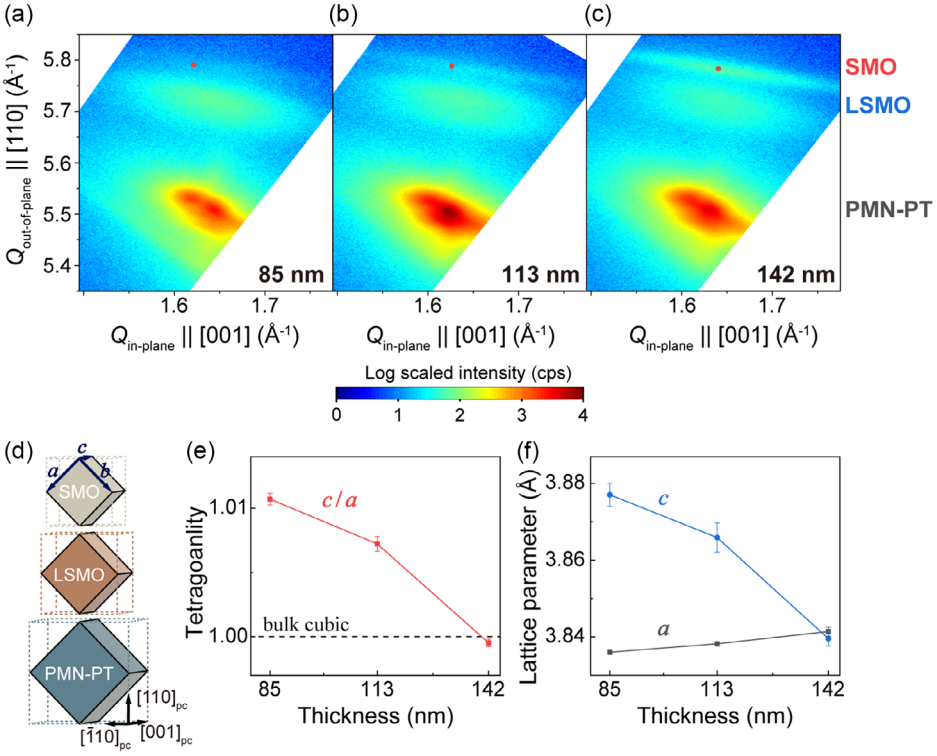

Figure 2. a) RSMs near $(321)_{pc}$ reflection of 85 nm, b) 113 nm, and c) 142 nm thick SMO film grown on LSMO/PMN-PT heterostructure. d) Schematic representation of unit cell of $(110)_{pc}$-oriented films on $(110)_{pc}$ PMN-PT substrate with pseudocubic lattice vector notation of $[110]_{pc}$, $[-110]_{pc}$, and $[001]_{pc}$. e) Measured lattice parameters and f) tetragonality, termed as *c*/*a* lattice constant ratio of SMO film as a function of SMO film thickness by comparing the peak position of $(110)_{pc}$ and $(321)_{pc}$ reflections.

The increase in film thickness resulted in a phase transition of the SMO film from the tetragonal to the cubic phase structure, as shown in Figure 2e. The *a*- and *c*-lattice parameters of 85 nm thick SMO film are 3.836 and 3.877 Å ($V = 57.05$ Å^3), while those for 142 nm thick film are 3.841 and 3.840 Å ($V = 56.65$ Å^3), as shown in Figure 2f. The tetragonality, defined by c/a ratios of the 85 and 142 nm thick SMO films, was 1.011 and 1.000, respectively. The strain relaxation behavior of epitaxial thin films can cause a decrease in the in-plane strain, resulting in a decrease in the *c*-lattice parameter of the film.[27] The in-plane tensile strain applied along the *c*-lattice of the 85 nm thick SMO film with the highest tetragonality in this study was 2.02%, which exceeded the DFT prediction of a 1% boundary strain to induce the ferroelectric phase.

The SMO film, regardless of film thickness, exhibits a larger unit cell volume due to a stretched lattice along three axes than the bulk cubic SMO structure ($a = 3.80$ and $V = 54.87$ Å^3).[31] This expansion in unit cell volume of SMO film under biaxial tensile strain can arise from the off-stoichiometry in $SrMnO_{3-\delta}$ ($\delta = 0$–0.5) due to the formation of $V_O^{\cdot\cdot}$. In most perovskite oxide thin films, strain-mediated defect formation causes an increase in the $V_O^{\cdot\cdot}$ concentration as the epitaxial strain increases.[32] When the $V_O^{\cdot\cdot}$ is formed in SMO film, the change in the Mn valence state from Mn^{4+} to Mn^{3+} can induce the volume expansion because the effective ionic radii of Mn^{3+} (0.645 Å) is larger than that of Mn^{4+} (0.53 Å).[33] The larger unit cell volume of the 85 nm thick SMO film, which was more strained than the 142 nm thick film, can be attributed to the higher $V_O^{\cdot\cdot}$ concentration in the 85 nm thick SMO film.

To clarify the $V_O^{\cdot\cdot}$ formation by strain, we performed XPS for the Mn $2p_{3/2}$ spectra, as shown in **Figure 3**a–c. The Gaussian-fitted Mn $2p_{3/2}$ spectra located at 641.6 and 642.6 eV in the XPS profile arise from the Mn valence states of 3+ and 4+, respectively.[34] The concentration of $V_O^{\cdot\cdot}$ was estimated by measuring the ratio of the integrated intensity of the Mn^{3+} to Mn^{4+} XPS profile (Mn^{3+}/Mn^{4+} ratio).[35] The Mn^{3+}/Mn^{4+} ratios for the SMO films with thicknesses of 85, 113, and 142 nm were determined to be 0.271, 0.269, and 0.266, respectively. A Mn^{3+}/Mn^{4+} ratio greater than zero signifies the presence of $V_O^{\cdot\cdot}$ within the SMO film, leading to the volumetric expansion observed in the RSM results. A higher Mn^{3+}/Mn^{4+} ratio of the 85 nm thick SMO film than that of thicker films indicates that the concentration of $V_O^{\cdot\cdot}$ increases with decreasing the thickness of SMO films due to the higher epitaxial strain, which is similar to the other epitaxial oxide film systems.[12] However, the difference in the measured thickness-dependent Mn^{3+}/Mn^{4+} ratios was very small and close to the error range (approximately 0.002), suggesting that a larger $V_O^{\cdot\cdot}$ concentration may be found near the interface of the SMO film.

The conventional XPS results were insufficient to investigate the $V_O^{\cdot\cdot}$ concentration along the depth because conventional XPS measurements are highly sensitive to the surface only. Depth profiles from EELS provided depth-dependent $V_O^{\cdot\cdot}$ concentrations. We collected EEL spectra at three different regions near the interface, middle, and surface of the 85 nm thick SMO film, denoted as regions **1**, **2**, and **3**, respectively (**Figure 4**a). The EELS spectrum near the oxygen K shell edge (O-K edge) shows three main peaks near 531, 538, and 544 eV, denoted as **a**, **b**, and **c** (Figure 4b), which arise from the hybridization of the unoccupied O 2*p* orbitals with the Mn 3*d*, Sr 4*d*, and Mn 4*sp* orbitals, respectively.[36–40] Integrated intensity ratio (**a**/**b**) and energy difference between the peaks **a** and **b** (ΔE) is important to investigate the Mn valence state because the formation of $V_O^{\cdot\cdot}$ changes the electron state of Mn 3d band occupancy.[30] Additionally, the ratio of the maximum intensities arising from the Mn-L_3 and L_2 edges (L_3/L_2 ratio), as shown in Figure 4c, allows for an accurate estimation of the Mn oxidation state involving the excitation of Mn 2*p* electrons into Mn 3*d* empty states.[41] Figure 4d–f shows the estimated depth-dependent nominal Mn oxidation states. The **a**/**b** peak ratio, ΔE, and L_3/L_2 ratio depending on Mn oxidation state of polycrystalline $SrMnO_3$ and $SrMnO_{2.5}$ reported in ref. [30] are shown in Figure 4d–f to emphasize their linear dependence. The average Mn valence states in regions **1**, **2**, and **3** were estimated to be +3.73, +3.87, and +3.87, respectively, indicating that the concentration of $V_O^{\cdot\cdot}$ near the interface between the SMO and LSMO films was higher than that in other regions. The higher $V_O^{\cdot\cdot}$ concentration near the interface is attributed to the relief of the high elastic energy generated by the highly strained region, which is consistent with a previous study in which the $V_O^{\cdot\cdot}$ concentration in the oxide film increased owing to the reduction in $V_O^{\cdot\cdot}$ formation energy.[27] Therefore, in highly strained thinner films, a high $V_O^{\cdot\cdot}$ concentration induces an overall unit cell volume expansion, in addition to the epitaxial strain expanding the in-plane lattice.

To observe the ferroelectric behavior expected due to the strain-mediated off-centering of cations within the tetragonal SMO thin film, we measured the piezoelectric response using DART-PFM. Measurement of the polarization voltage (*P*–*V*)

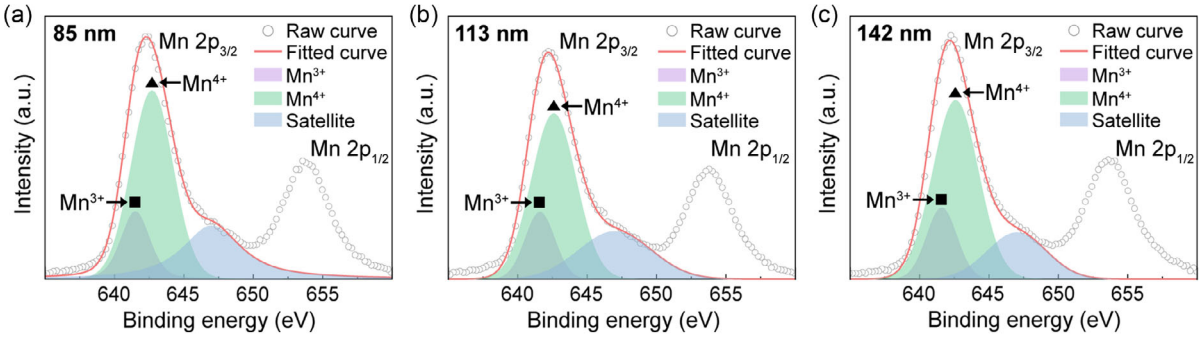

Figure 3. a) Mn $2p_{3/2}$ spectra of 85 nm, b) 113 nm, and c) 142 nm thick SMO films grown on LSMO/PMN-PT substrate.

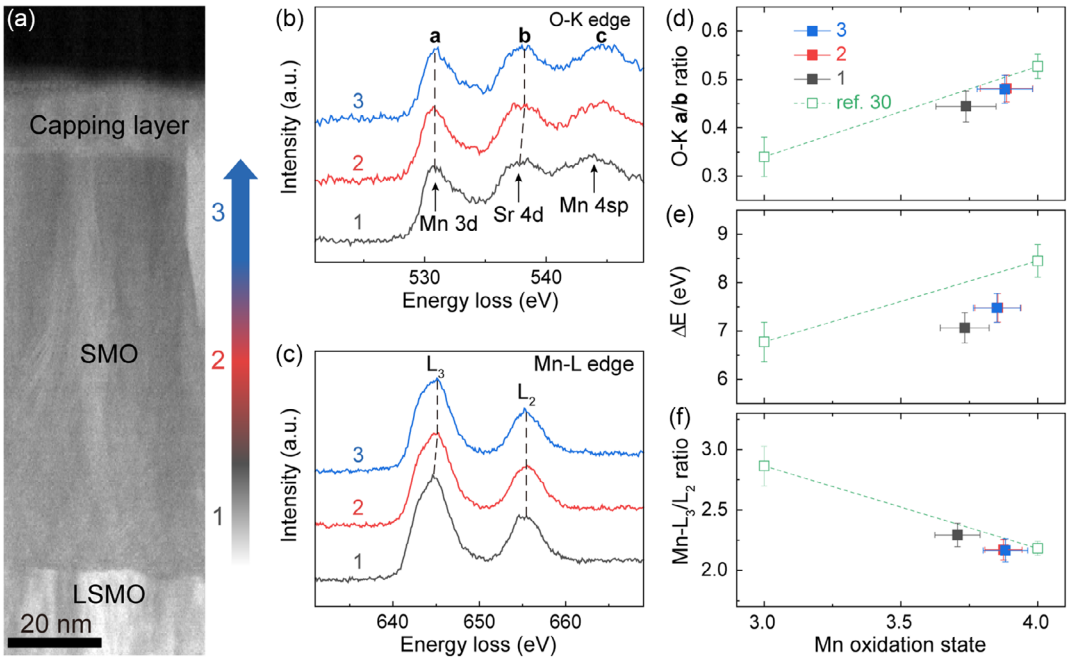

Figure 4. a) Cross-sectional TEM image of the 85 nm thick SMO film showing the regions where the depth profiles of EEL spectra were measured. Comparison of EEL spectra showing the b) O-K edge and c) Mn-L edge. The quantitative analysis of the Mn oxidation state from d) the normalized prepeak intensity, e) the energy distance between the prepeak and main peak position, and f) the area ratio of Mn L_3 and L_2 edge by applying the procedure as reported.[41] For comparison, the previously reported EEL spectra result of a comparison of polycrystalline $SrMnO_3$ and $SrMnO_{2.5}$ are shown with open squares and dashed lines.[30]

for the ferroelectric hysteresis loops and advanced in situ XRD for the piezoelectric response were not feasible owing to the high leakage current density of the 85 nm thick SMO film, as shown in Figure S1 (Supporting Information). The surface topography of the SMO film exhibited long-range stripe patterns, as shown in **Figure 5**a, which is a distinctive feature of the $(110)_{pc}$-oriented epitaxial film. These striped features were aligned in the in-plane $[001]_{pc}$ direction of the underlying substrate.[42,43] Interestingly, we claim that the 85 nm thick SMO film contains both in-plane and out-of-plane polarized domains, as shown in Figure 5b–e. The polarized domains were randomly distributed, showing a distinct amplitude of the piezoelectric response. When comparing the lateral and vertical amplitude images, two types of domains exist: 1) regions with lateral amplitude and almost zero vertical amplitude, and 2) regions with both lateral and vertical amplitudes.

The polarization switching behavior, which is a primitive characteristic of ferroelectrics, was examined to clarify the ferroelectricity of the SMO film. The local PFM amplitude and phase hysteresis loop along vertical direction were obtained by applying AC voltage (V_{ac}) of 2 V at each DC voltage (V_{dc}) step with the sweep range from 0, −8, 0, 8 to 0 V. The lateral PFM hysteresis loop was restricted because of the difficulties in calibrating the lateral component from the noise signal and tip damage. The SMO film exhibits a butterfly-shaped amplitude loop except in the bias range from 0 to 4 V and had phase reversals of nearly 180° at around −5 and 4 V, as shown in Figure 5e,f, respectively. The amplitude was not saturated, but increased after the phase reversals. This may be attributed to the electrostatic interaction between the cantilever and the sample or the Joule heating effect from the current flow, because the voltage bias pulse effect could remain when the amplitude was measured owing to the relatively narrow width of the voltage pulse (5 ms).[44] Although it is difficult to remove this noise, the measured switchability of polarization by external electric fields confirms the existence of switchable ferroelectric properties in the 85 nm thick single-crystal $(110)_{pc}$-oriented SMO film.

The measured ferroelectricity of the SMO film is suspected to arise from the interplay between strain and defect chemistry engineering. While strain-induced polarization in perovskite oxide films is generally predicted to be parallel to the strain axis,[8,9] an 85 nm thick SMO film grown on a $(110)_{pc}$-oriented LSMO/PMN-PT substrate exhibited ferroelectric domains consisting of in-plane and out-of-plane polarizations. As discussed above, the 85 nm thick SMO film exhibited volume expansion with an elongated lattice along all three axes due to the formation of $V_O^{\cdot\cdot}$. Ferroelectricity is known to be modulated by tuning the crystal lattice,[12] indicating that unusual ferroelectric properties can arise from an abnormally expanded lattice due to oxygen deficiency. It would be useful to discuss similar results in the literature. For instance, in the case of (110)-$SmFeO_{3-\delta}$ film showing extension along *a*-, *b*-, and *c*-axes under the biaxial tensile strain, lattice distortion derived by the $V_O^{\cdot\cdot}$ in Fe–O layer induces polar displacement along the out-of-plane [-1-10] direction.[45]

The converse piezoelectric effect of the PMN-PT substrate changed the biaxial strain of the SMO film. In situ synchrotron XRD measurements were employed to monitor the changes in

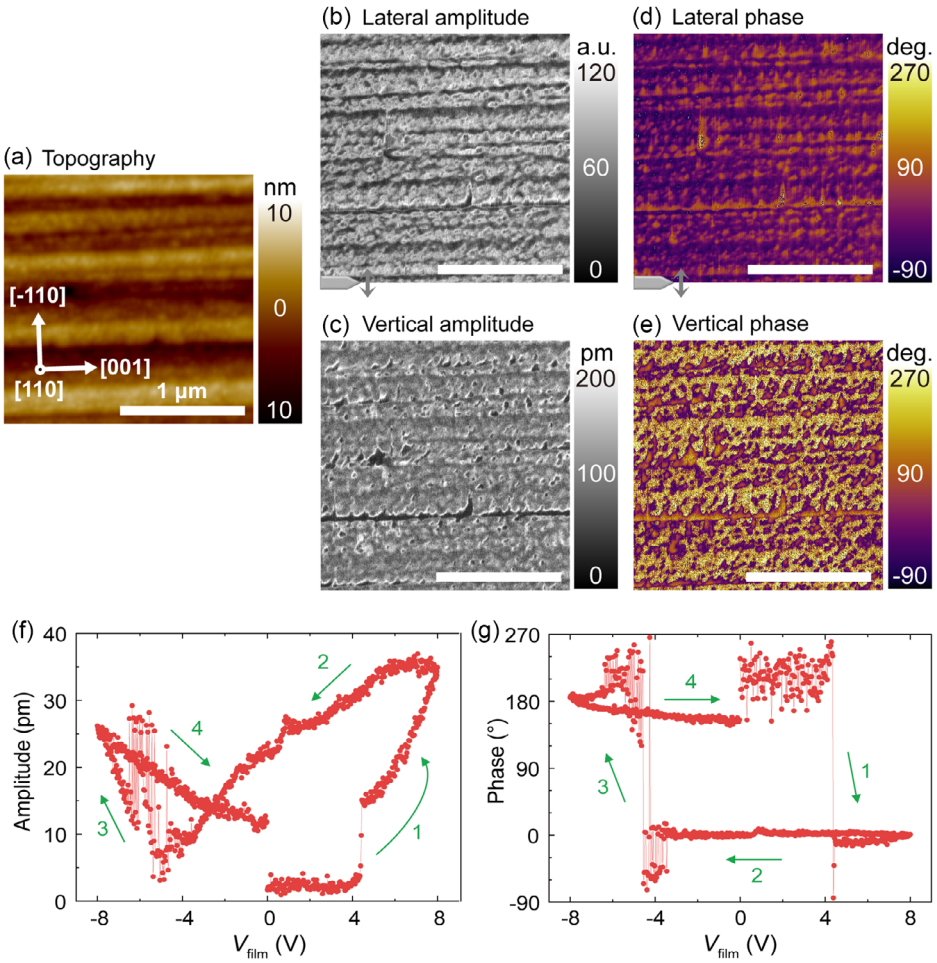

Figure 5. a) Surface topography of 85 nm thick $(110)_{pc}$-oriented $SrMnO_3$ thin film with corresponding dual AC resonance tracking piezoelectric force microscopy (DART-PFM) b,c) vertical and lateral amplitude, and d,e) vertical and lateral phase. f) Vertical analysis of DART-PFM amplitude and g) phase hysteresis loop.

the $(110)_{pc}$ reflection of both the PMN-PT substrate and the SMO film under the application of an electric field to the PMN-PT substrate (E_{sub}) along the $[110]_{pc}$ direction. The $(110)_{pc}$ reflection peaks from both the LSMO bottom electrode and SMO film were individually fitted using two Gaussian functions. Under E_{sub}, the peak position of $(110)_{pc}$ reflection from PMN-PT substrate shifts toward the lower 2theta angle due to the increase in $d_{(110)}$-spacing, as shown in **Figure 6**a. The LSMO and SMO films also exhibit a shift in the $(110)_{pc}$ reflection peak toward the lower 2theta values, as shown in Figure 6b, indicating a piezoelectric response from the PMN-PT substrate leads to a lattice distortion of the LSMO and SMO films. The piezoelectric response of PMN-PT with different magnitudes of E_{sub} exhibited a V-shaped curve, as shown in Figure 6c, owing to the polarization reversal effect. Because the piezoelectric strain of the PMN-PT substrate was transferred to the SMO film, we found similar V-shaped strain curves, as shown in Figure 6d.

The electrically induced lattice deformation parallel (ε_{out}) and perpendicular (ε_{in}) to the electric field direction was calculated for a quantitative assessment of the transferred piezoelectric strain, as shown in Figure 6e,f, respectively. The ε_{out} was calculated using the expression, $[d(E) - d(0)]/d(0)$, wherein $d(E)$ and $d(0)$ are the $d_{(110)}$-spacing under the application of E_{sub} and zero electric field conditions. The calculated ε_{out} for the PMN-PT substrate and SMO film are 0.109% and 0.057% at $-8\,kV\,cm^{-1}$, and 0.093% and 0.061% at $8\,kV\,cm^{-1}$, respectively. By employing the Poisson equation, ε_{in} can be estimated by the relationship derived from elastic deformation, $\varepsilon_{in} = ((1-\nu)/(2\nu))\varepsilon_{out}$, where ν represents the Poisson's ratio ($\nu_{PMN-PT} = 0.3$,[46] $\nu_{LSMO} = 0.29$,[47] and $\nu_{SMO} = 0.24$[28]). The estimated ε_{in} for the PMN-PT substrate and SMO film are 0.127% and 0.092% at $-8\,kV\,cm^{-1}$, and 0.109% and 0.098% at $8\,kV\,cm^{-1}$, respectively. Up to 90% of the piezoelectric strain of the PMN-PT substrate was transferred to the SMO film, which indicates strong interfacial mechanical coupling between the film and substrate. As discussed above, the depth profiles of the EEL spectra exhibit a large $V_O^{\cdot\cdot}$ concentration near the interface. The strain-mediated $V_O^{\cdot\cdot}$ induced lattice expansion relieved the elastic energy caused by the misfit strain, resulting in the accommodation of the epitaxial strain without relaxation. We would like to emphasize that the polarization of the SMO film can be controlled and enhanced by adjusting the

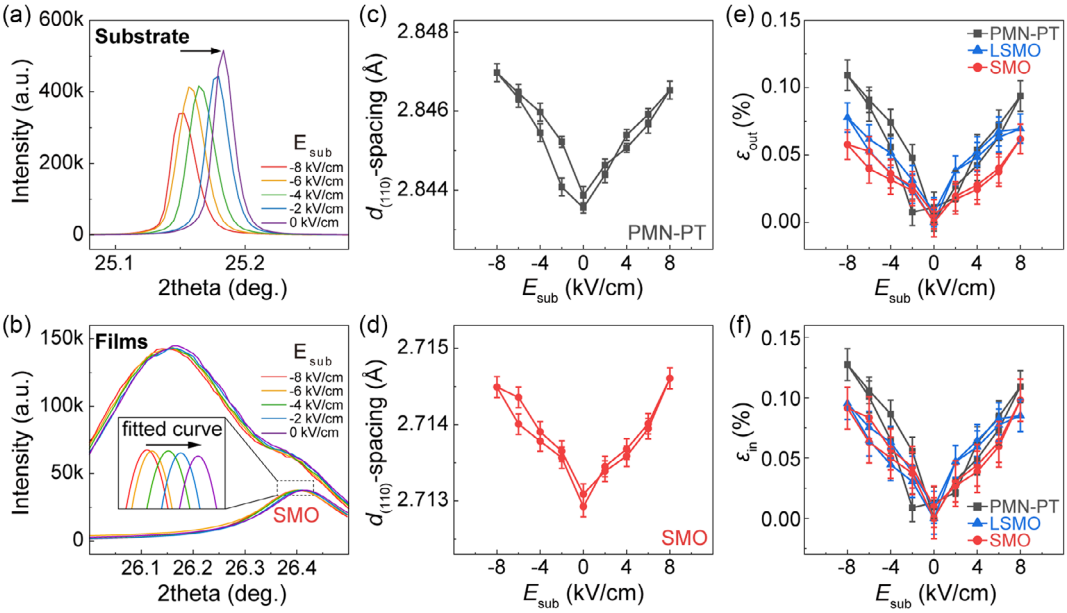

Figure 6. a) XRD profiles near $(110)_{pc}$ reflection of the PMN-PT substrate and b) film region with fitted curves of SMO film, when the amplitude of electric field applied to the substrate is varied from −8 to 0 kV cm^{-1}. The electric field was applied along the out-of-plane $[110]_{pc}$ direction of PMN-PT substrate. The inset in (b) is the enlarged profiles of fitted SMO curves. The calculated d-spacing along the out-of-plane $[110]_{pc}$ direction of c) PMN-PT substrate and d) SMO film. The measured strain of the PMN-PT substrate (black squares), LSMO bottom electrode (blue triangles), and SMO film (red circles) e) parallel and f) perpendicular to applied electric field to the PMN-PT substrate.

piezoelectric strain of the PMN-PT substrate because of the strong lattice-charge coupling predicted from DFT calculations.[8,9] To measure the variation in the piezoelectric response of the SMO film with changes in the biaxial direction, we attempted to measure the changes in $d_{(110)}$-spacing of the SMO film by applying an electric field to the SMO thin film and PMN-PT substrate simultaneously using an advanced X-ray scattering technique (Figure S7, Supporting Information). Although the observed shifts in the diffraction peak of the SMO film were notably small owing to unexpected hindrances that occurred during the measurement, such as substantial leakage current, we anticipate that the piezoelectric response of the PMN-PT substrate can control the ferroelectric polarization of the SMO film.[48]

3. Conclusion

SMO thin films were successfully grown on a $(110)_{pc}$-oriented piezoelectric PMN-PT substrate with a LSMO bottom electrode layer. The SMO thin film showed a tensile strain along the in-plane c-lattice as large as 2.02%, which was sufficient to induce a ferroelectric phase. The high concentration of oxygen vacancies produced by the high elastic energy mediated the overall expansion of the volume of the unit cell. PFM revealed the coexistence of ferroelectric domains with in-plane and out-of-plane polarizations in the SMO thin film on the PMN-PT substrate. Using the piezoelectric response of the PMN-PT substrate, the application of an electric field to the PMN-PT substrate enabled the manipulation of the biaxial strain of the SMO film. The crystalline quality of the (110)-oriented SMO films should be significantly enhanced to gain deeper insights into the formation of the ferroelectric phases and in situ strain engineering. This study underscores the potential for electric field manipulation to control the strain in thin films, opening avenues for further exploration and application in the field of ferroelectric materials.

4. Experimental Section

Sample Preparation: SMO/LSMO heterostructures were grown on a (110)-oriented PMN-PT ($x = 0.3$) substrate using PLD. The SRO capping layer was grown on the SMO film to improve the postannealing effect.[15] The substrate temperature was maintained at 700 °C for LSMO, and 670 °C for SMO and SRO. The incident angle of the KrF excimer laser (248 nm) on the target was 45°. The distance between the target and the substrate was fixed at 5 cm. The growth conditions were optimized with a laser fluence of 0.8 J cm^{-2} and a frequency of 4 Hz. The laser fluence was set to minimize the formation of off-stoichiometry since the different cation stoichiometry can induce the lattice distortion. The oxygen partial pressure was varied from 1 to 100 mTorr. The film thickness was controlled by varying the number of laser pulses. The thicknesses of LSMO and SRO were fixed at 30 and 20 nm, respectively. To minimize leakage current and oxygen vacancies, the SMO films were annealed at 350 °C under the dynamic O_2 pressure of 760 Torr for 1 h. The SRO capping layer was removed after annealing.

Structural Characterization: The orientation, crystallinity, and strain state were investigated using XRD with 10 keV photon energy at the 9C beamline of the Pohang Accelerator Laboratory (PAL). RSMs near the (110) and (321) reflections were obtained by collecting the diffracted X-ray beams using a gated pixel array detector (Pilatus 100 K, Dectris). XPS (NEXSA G2, Thermo Fisher Scientific) and cross-sectional transmission electron microscopy (TEM)-EELS (Tecnai G2 F30 S-Twin, FEI) were used to analyze the oxygen stoichiometry of the SMO film. The samples for TEM were prepared by focused ion beam (NX5000, Hitachi) milling. The SRO capping

layer was preserved to avoid air degradation during sampling for XPS and EELS measurements. For the XPS analysis, the core-level spectra were fitted using a Gaussian function after subtracting the Shirley background. The measured EEL spectra were Gaussian fitted after subtracting the background using a power-law fit. The Mn-L spectra were additionally scaled using a Hartree–Slater cross-section function before fitting to remove the continuum contribution.

Piezoelectric Response Hysteresis Loop Measurement: The piezoelectric response of the SMO film was measured by DART-PFM using a commercial scanning probe microscope (MFP-Infinity, Asylum Research). The PFM hysteresis loops were measured using conductive Cr/Pt-coated cantilevers (Multi75E-G, BudgetSensors) with a resonant frequency of approximately 68 kHz and a spring constant of approximately 3 N m^{-1}, while applying triangle–square waveforms sweeping the voltage pulses with a pulse width of 5 ms from 0, 8, 0, −8 to 0 V over 20 s, accompanied by an AC bias voltage of 2 V to the tip around the contact resonant frequency of approximately 337 kHz. The amplitude and phase were measured when no DC bias voltage pulse was applied (off-field mode or pulsed DC mode) to exclude the electrostatic force between the tip and the sample. The amplitude was calibrated using the inverse optical lever sensitivity calculated from the force–distance curve and adjusted by the quality factor based on the simple harmonic oscillator model because the amplitude was amplified by the resonance of the cantilever.

Supporting Information

Supporting Information is available from the Wiley Online Library or from the author.

Acknowledgements

J.Y.J. acknowledges support through grants from the National Research Foundation of Korea (NRF) funded by the Korean government (NRF-2017M3D1A1040828, NRF-2020R1A2C2006127, and NRF-2021R1A5A1032996) and GIST Research Institute (GRI) grant funded by GIST. H.J.L. acknowledges the support by 2023 Research Grant from Kangwon National University and by "Regional Innovation Strategy (RIS)" through the National Research Foundation of Korea (NRF) funded by the Ministry of Education (MOE) (2022RIS-005). S.H. acknowledges the support of the National Research Foundation of Korea (NRF) grant funded by the Korea government (MSIT) (RS-2023-00247245). C.-H.Y. acknowledges the support of the NRF grant via the Creative Research Center for Lattice Defectronics (grant no. NRF-2017R1A3B1023686).

Conflict of Interest

The authors declare no conflict of interest.

Data Availability Statement

The data that support the findings of this study are available from the corresponding author upon reasonable request.

Keywords

$(1-x)Pb(Mg_{1/3}Nb_{2/3})O_3$–$xPbTiO_3$ substrates, defect chemistry, ferroelectrics, pulsed laser deposition, $SrMnO_3$ film

Received: January 18, 2024
Revised: March 21, 2024
Published online: April 24, 2024

[1] N. A. Hill, *J. Phys. Chem. B* **2000**, *104*, 6694.
[2] L. Weston, X. Y. Cui, S. P. Ringer, C. Stampfl, *Phys. Rev. B* **2016**, *93*, 165210.
[3] W. Eerenstein, N. D. Mathur, J. F. Scott, *Nature* **2006**, *442*, 759.
[4] C. N. R. Rao, C. R. Serrao, *J. Mater. Chem.* **2007**, *17*, 4931.
[5] H. Sim, J. Jeong, H. Kim, S. W. Cheong, J.-G. Park, *J. Phys.: Condens. Matter* **2018**, *30*, 105601.
[6] C. R. Serrao, A. Sundaresan, C. N. R. Rao, *J. Phys.: Condens. Matter* **2007**, *19*, 496217.
[7] K. Chapagain, D. E. Brown, S. Kolesnik, S. Lapidus, B. Haberl, J. Molaison, C. Lin, C. Kenney-Benson, C. Park, J. Pietosa, E. Markiewicz, B. Andrzejewski, J. W. Lynn, S. Rosenkranz, B. Dabrowski, O. Chmaissem, *Phys. Rev. Mater.* **2019**, *3*, 084401.
[8] J. H. Lee, K. M. Rabe, *Phys. Rev. Lett.* **2010**, *104*, 207204.
[9] A. Edström, C. Ederer, *Phys. Rev. Mater.* **2018**, *2*, 104409.
[10] A. Marthinsen, C. Faber, U. Aschauer, N. A. Spaldin, S. M. Selbach, *MRS Commun.* **2016**, *6*, 182.
[11] H. Sakai, J. Fujioka, T. Fukuda, D. Okuyama, D. Hashizume, F. Kagawa, H. Nakao, Y. Murakami, T. Arima, A. Q. Baron, Y. Taguchi, Y. Tokura, *Phys. Rev. Lett.* **2011**, *107*, 137601.
[12] J. Hwang, Z. Feng, N. Charles, X. R. Wang, D. Lee, K. A. Stoerzinger, S. Muy, R. R. Rao, D. Lee, R. Jacobs, D. Morgan, Y. Shao-Horn, *Mater. Today* **2019**, *31*, 100.
[13] C. Becher, L. Maurel, U. Aschauer, M. Lilienblum, C. Magen, D. Meier, E. Langenberg, M. Trassin, J. Blasco, I. P. Krug, P. A. Algarabel, N. A. Spaldin, J. A. Pardo, M. Fiebig, *Nat. Nanotechnol.* **2015**, *10*, 661.
[14] R. Guzman, L. Maurel, E. Langenberg, A. R. Lupini, P. A. Algarabel, J. A. Pardo, C. Magen, *Nano Lett.* **2016**, *16*, 2221.
[15] H. An, Y.-G. Choi, Y.-R. Jo, H. J. Hong, J.-K. Kim, O. Kwon, S. Kim, M. Son, J. Yang, J.-C. Park, H. Choi, J. Lee, J. Song, M.-H. Ham, S. Ryu, Y. Kim, C. W. Bark, K.-T. Ko, B.-J. Kim, S. Lee, *NPG Asia Mater.* **2021**, *13*, 69.
[16] J. W. Guo, P. S. Wang, Y. Yuan, Q. He, J. L. Lu, T. Z. Chen, S. Z. Yang, Y. J. Wang, R. Erni, M. D. Rossell, V. Gopalan, H. J. Xiang, Y. Tokura, P. Yu, *Phys. Rev. B* **2018**, *97*, 235135.
[17] D. G. Schlom, L.-Q. Chen, X. Pan, A. Schmehl, M. A. Zurbuchen, *J. Am. Ceram.* **2008**, *91*, 2429.
[18] J. M. Rondinelli, N. A. Spaldin, *Adv. Mater.* **2011**, *23*, 3363.
[19] S. Dhole, A. Chen, W. Nie, B. Park, Q. Jia, *Nanomaterials* **2022**, *12*, 835.
[20] S. Zhang, Y. G. Zhao, P. S. Li, J. J. Yang, S. Rizwan, J. X. Zhang, J. Seidel, T. L. Qu, Y. J. Yang, Z. L. Luo, Q. He, T. Zou, Q. P. Chen, J. W. Wang, L. F. Yang, Y. Sun, Y. Z. Wu, X. Xiao, X. F. Jin, J. Huang, C. Gao, X. F. Han, R. Ramesh, *Phys. Rev. Lett.* **2012**, *108*, 137203.
[21] L. Yang, Y. Zhao, S. Zhang, P. Li, Y. Gao, Y. Yang, H. Huang, P. Miao, Y. Liu, A. Chen, C. W. Nan, C. Gao, *Sci. Rep.* **2014**, *4*, 4591.
[22] X. Liu, M. Zheng, J. Yang, P. Guan, F. Zhang, Y. Wang, H. Ni, *Phys. Status Solidi RRL* **2022**, *16*, 2100474.
[23] F. Li, S. Zhang, D. Damjanovic, L. Q. Chen, T. R. Shrout, *Adv. Funct. Mater.* **2018**, *28*, 1801504.
[24] H. Wang, X. Jiang, Y. Wang, R. W. Stark, P. A. van Aken, J. Mannhart, H. Boschker, *Nano Lett.* **2020**, *20*, 88.
[25] C. Ricca, I. Timrov, M. Cococcioni, N. Marzari, U. Aschauer, *Phys. Rev. B* **2019**, *99*, 094101.
[26] J. Bai, Q. Liu, M. Wu, J. Yang, W. Jiang, J. Wang, W. Bai, Y. Zhang, X. Tang, J. Chu, *Appl. Phys. Lett.* **2020**, *116*, 142901.
[27] E. Langenberg, L. Maurel, G. Antorrena, P. A. Algarabel, C. Magen, J. A. Pardo, *ACS Omega* **2021**, *6*, 13144.
[28] P. Agrawal, J. Guo, P. Yu, C. Hébert, D. Passerone, R. Erni, M. D. Rossell, *Phys. Rev. B* **2016**, *94*, 104101.
[29] T. Wu, P. Zhao, M. Bao, A. Bur, J. L. Hockel, K. Wong, K. P. Mohanchandra, C. S. Lynch, G. P. Carman, *J. Appl. Phys.* **2011**, *109*, 124101.

[30] S. Kobayashi, Y. Tokuda, T. Mizoguchi, N. Shibata, Y. Sato, Y. Ikuhara, T. Yamamoto, *J. Appl. Phys.* **2010**, *108*, 124903.
[31] T. Takeda, S. Ōhara, *J. Phys. Soc. Jpn* **1974**, *37*, 275.
[32] A. Herklotz, D. Lee, E. J. Guo, T. L. Meyer, J. R. Petrie, H. N. Lee, *J. Phys.: Condens. Matter* **2017**, *29*, 493001.
[33] U. Aschauer, R. Pfenninger, S. M. Selbach, T. Grande, N. A. Spaldin, *Phys. Rev. B* **2013**, *88*, 054111.
[34] A. K. Mandal, G. Panchal, S. Chowdhury, A. Jana, R. J. Choudhary, D. M. Phase, *J. Supercond.* **2019**, *33*, 1633.
[35] F. Wang, Y. Q. Zhang, Y. Bai, W. Liu, H. R. Zhang, W. Y. Wang, S. K. Li, S. Ma, X. G. Zhao, J. R. Sun, Z. H. Wang, Z. J. Wang, Z. D. Zhang, *Appl. Phys. Lett.* **2016**, *109*, 052403.
[36] G. Zampieri, F. Prado, A. Caneiro, J. Briático, M. T. Causa, M. Tovar, B. Alascio, M. Abbate, E. Morikawa, *Phys. Rev. B* **1998**, *58*, 3755.
[37] M. Abbate, F. M. de Groot, J. C. Fuggle, A. Fujimori, O. Strebel, F. Lopez, M. Domke, G. Kaindl, G. A. Sawatzky, M. Takano, Y. Takeda, H. Eisaki, S. Uchida, *Phys. Rev. B* **1992**, *46*, 4511.
[38] H. Kurata, C. Colliex, *Phys. Rev. B.* **1993**, *48*, 2102.
[39] H. L. Ju, H. C. Sohn, K. M. Krishnan, *Phys. Rev. Lett.* **1997**, *79*, 3230.
[40] T. Mizoguchi, W. Olovsson, H. Ikeno, I. Tanaka, *Micron* **2010**, *41*, 695.
[41] M. Varela, M. P. Oxley, W. Luo, J. Tao, M. Watanabe, A. R. Lupini, S. T. Pantelides, S. J. Pennycook, *Phys. Rev. B* **2009**, *79*, 085117.
[42] P. C. Wu, C. C. Wei, Q. Zhong, S. Z. Ho, Y. D. Liou, Y. C. Liu, C. C. Chiu, W. Y. Tzeng, K. E. Chang, Y. W. Chang, J. Zheng, C. F. Chang, C. M. Tu, T. M. Chen, C. W. Luo, R. Huang, C. G. Duan, Y. C. Chen, C. Y. Kuo, J. C. Yang, *Nat. Commun.* **2022**, *13*, 2565.
[43] P. Perna, C. Rodrigo, E. Jiménez, F. J. Teran, N. Mikuszeit, L. Méchin, J. Camarero, R. Miranda, *J. Appl. Phys.* **2011**, *110*, 013919.
[44] B. Kim, D. Seol, S. Lee, H. N. Lee, Y. Kim, *Appl. Phys. Lett.* **2016**, *109*, 102901.
[45] H. Li, Y. Yang, S. Deng, L. Zhang, S. Cheng, E. J. Guo, T. Zhu, H. Wang, J. Wang, M. Wu, P. Gao, H. Xiang, X. Xing, J. Chen, *Sci. Adv.* **2022**, *8*, eabm8550
[46] W. Hou, S. A. Chowdhury, A. Dey, C. Watson, T. Peña, A. Azizimanesh, H. Askari, S. M. Wu, *Phys. Rev. Appl.* **2022**, *17*, 024013.
[47] F. Sandiumenge, J. Santiso, L. Balcells, Z. Konstantinovic, J. Roqueta, A. Pomar, J. P. Espinos, B. Martinez, *Phys. Rev. Lett.* **2013**, *110*, 107206.
[48] H. J. Lee, E.-J. Guo, J. H. Kwak, S. H. Hwang, K. Dörr, J. H. Lee, J. Y. Jo, *Appl. Phys. Lett.* **2017**, *110*, 032901.